

Electron Beam Melting Technology Improvements



**CRADA FINAL REPORT
NFE-12-04045**

**Approved for Public Release.
Distribution is Unlimited.**

Ryan R. Dehoff
January 18, 2019

DOCUMENT AVAILABILITY

Reports produced after January 1, 1996, are generally available free via US Department of Energy (DOE) SciTech Connect.

Website www.osti.gov

Reports produced before January 1, 1996, may be purchased by members of the public from the following source:

National Technical Information Service
5285 Port Royal Road
Springfield, VA 22161
Telephone 703-605-6000 (1-800-553-6847)
TDD 703-487-4639
Fax 703-605-6900
E-mail info@ntis.gov
Website <http://classic.ntis.gov/>

Reports are available to DOE employees, DOE contractors, Energy Technology Data Exchange representatives, and International Nuclear Information System representatives from the following source:

Office of Scientific and Technical Information
PO Box 62
Oak Ridge, TN 37831
Telephone 865-576-8401
Fax 865-576-5728
E-mail reports@osti.gov
Website <http://www.osti.gov/contact.html>

This report was prepared as an account of work sponsored by an agency of the United States Government. Neither the United States Government nor any agency thereof, nor any of their employees, makes any warranty, express or implied, or assumes any legal liability or responsibility for the accuracy, completeness, or usefulness of any information, apparatus, product, or process disclosed, or represents that its use would not infringe privately owned rights. Reference herein to any specific commercial product, process, or service by trade name, trademark, manufacturer, or otherwise, does not necessarily constitute or imply its endorsement, recommendation, or favoring by the United States Government or any agency thereof. The views and opinions of authors expressed herein do not necessarily state or reflect those of the United States Government or any agency thereof.

ORNL/TM-2019/1092
CRADA/NFE-12-04045

MANUFACTURING DEMONSTRATION FACILITY
Materials Science and Technology Division

ELECTRON BEAM MELTING TECHNOLOGY IMPROVEMENTS

Ryan R Dehoff
Michael M. Kirka
Elizabeth Ellis
Vincent Paquit
Peeyush Nandwana
Alexander Plotkowski

Date Published:
January 18, 2019

Prepared by
OAK RIDGE NATIONAL LABORATORY
Oak Ridge, TN 37831-6283
managed by
UT-BATTELLE, LLC
for the
US DEPARTMENT OF ENERGY
under contract DE-AC05-00OR22725

CONTENTS

CONTENTS.....	III
TABLE OF FIGURES.....	IV
ACKNOWLEDGEMENTS.....	V
ABSTRACT.....	1
1. TECHNICAL SUMMARY.....	1
1.1 QUALIFICATION.....	2
1.1.1 IN-SITU MONITORING.....	2
1.1.2 DATA TOOLS.....	3
1.2 MICROSTRUCTURE CONTROL.....	4
1.3 HIGH-TEMPERATURE MATERIALS.....	8
1.4 SUMMARY.....	11
2. PUBLICATIONS.....	12

TABLE OF FIGURES

Figure 1. EBM applications: Left, hydraulic hand [1], Right, BALD bracket [2].	1
Figure 2. NIR temperature calibration. Left: original; right: calibrated. From [3].	2
Figure 3. In-situ porosity detection. (a) Pore count per layer as a function of layer number for Powder B (shades of blue) having large number of pores per layer compared to Powders A (shades of red) and C (shades of green). (b, c) The correlation between pore diameter and failure site of the sample (Color figure online). (From [5]).	3
Figure 4. The main analysis window (left) in Falcon consists of a set of interactive data visualizations that allow users to explore temporal and statistical patterns in time series data for multiple variables. The center variable visualization panel features both overview and detail visualizations. When time range selections are set (see the three rectangles with yellow borders in the BeamCurrent variable pane), a statistical summary pane is added to the selection details panel at right to summarize the selected data. From the main window, the user can access two additional analysis windows, which provide more detailed views of segments derived from the entire time series of a particular variable.	3
Figure 5: EDEN interface showing key variables.	4
Figure 8. Crystallographic orientation map corresponding to inverse pole figure for fcc nickel obtained on cross-section of EBM build obtained through EBSD. The bulk shows $\langle 001 \rangle$ columnar solidification grain growth, the outline of the letters show equiaxed grain growth indicated by lack of any significant $\langle 001 \rangle$ component, and the interior areas of letters D, O and E exhibit a mixture of $\langle 001 \rangle$ growth with the solidification map for Inconel 718 describing the estimated ranges for G and R for each of scan strategies overlaid. From [9].	5
Figure 9. Exploded view of the point heat source fill detailing the fill of points. (a) the first and second points in each row set, (b) the fill of the first row set, (c) fill of subsequent rows. From [10].	5
Figure 10. Change in temperature gradient (G) and liquid-solid interface velocity (R) of spot melt as a function of (a) preheat temperature, (b) spot ON time, (c) beam diameter, and (d) spot beam current. From [12].	6
Figure 11. A snapshot of the simulated surface melt pools for the (a) cube 15 and (b) cube 16 processing conditions. (c) Values of predicted G and R overlaid on top of the CET curve for alloy 718. From [13].	7
Figure 12. Completed EB-PBF alloy 718 bracket build with equiaxed grain formation in the spot melt region and columnar grain formation in the raster melt region. From [13].	7
Figure 13. Optical micrograph of the microstructure gradient observed at the top of EBM Inconel 718 block with the three distinct regions discernible. From [16].	8
Figure 14. Aluminum and titanium content of common Ni-base superalloys in relation to their susceptibility to cracking.	9
Figure 15. Tensile properties of post-processed EBM Mar-M247 at various temperature from room temperature through 950°C.	10
Figure 16. Evolution of (a) temperature distribution, (b) thermal stress (only tensile stresses are shown and therefore color images indicate as force imbalance), and (c) susceptible temperature range ($f_s = 0.7$ at 1623 K and $f_s = 0.98$ at 1498 K) during horizontal scanning. Hot cracking occurs at the intersection of the susceptible temperature range and high at the left edge (S22 is along y-direction). From [22].	10

ACKNOWLEDGEMENTS

This CRADA NFE-12-04045 was conducted as a project within the Oak Ridge National Laboratory (ORNL) Manufacturing Demonstration Facility (MDF) sponsored by the US Department of Energy Advanced Manufacturing Office (CPS Agreement Number 24765).. Research sponsored by the U.S. Department of Energy, Office of Energy Efficiency and Renewable Energy, Advanced Manufacturing Office, under contract DE-AC05-00OR22725 with UT-Battelle, LLC.

ABSTRACT

ORNL and Arcam AB have collaborated to improve and broaden the application and dissemination of electron beam melting (EBM) technology. While EBM is a promising additive manufacturing technology with the potential to revolutionize many industries, several issues prevent its widespread adoption at an industrial scale. In collaboration with Arcam, ORNL researchers have worked to improve the reliability of EBM processes using in-situ monitoring methods and data analytics, developed new scan strategies to allow site-specific microstructure control, and expanded EBM technologies to high-temperature materials. This report details the results of this collaboration.

1. TECHNICAL SUMMARY

This Manufacturing Demonstration Facility (MDF) CRADA project was begun on July 18, 2012 and was completed on July 18, 2018. The collaboration partner is Arcam AB.

Electron beam melting (EBM) is a powder bed additive manufacturing (AM) process that uses an electron beam to melt a thin layer of metal powder in a site-specific manner. The area melted in each layer is determined by slicing a computer-aided drawing file into layers, which are consecutively added to produce three-dimensional objects. The EBM technology yields nearly unlimited component design flexibility and has the potential to reduce manufacturing energy and material waste. ORNL researchers, in collaboration with Arcam AB, have used the EBM process for a variety of novel manufacturing applications, including the fabrication of lightweight mesh robotic arms with incorporated fluidics [1], aerospace brackets made using significantly reduced material outlay [2], and gas turbine components from non-weldable alloys. A few of these applications are shown in Figure 1.



Figure 1. EBM applications: Left, hydraulic hand [1], Right, BALD bracket [2].

The EBM technology has the potential to revolutionize how complex components are manufactured in a variety of industries, including medical, aerospace, automotive industries. However, successful deployment of the EBM process at industrial scales requires improved reliability of the deposition process, increased control over final microstructures and properties, and expansion to new and industrially relevant materials. These were the goals on which the ORNL/Arcam AB collaboration was based.

1.1 QUALIFICATION

AM has demonstrated the ability to fabricate fully functional complex components at reduced production costs and significant material and energy savings, as well as the potential to decrease component lead times and to fabricate complex designs not possible through conventional processing technologies. Despite these advantages, metal AM technologies have not yet been widely adopted by the industrial sector. This is partially because information pertaining to the mechanical integrity of components remains poorly understood. In particular, component certification methodologies have not been adopted, meaning that most AM development follows a trial-and-error methodology, negating the potential benefits of rapid prototyping and reduced material costs.

1.1.1 In-situ monitoring

In-situ monitoring of AM processes can dramatically improve reliability. Using high-speed IR and near-IR (NIR) data, the melt area of each layer can be studied, enabling detection of porosity and cracking throughout a build. First, a method was developed for properly calibrating temperature profiles from thermographic data to account for the emittance change during melting, and to identify the transition of material from metal powder to a solid as-printed part. A corrected temperature profile was then assembled for each point using calibrations for these surface conditions [3], as shown in Figure 2.

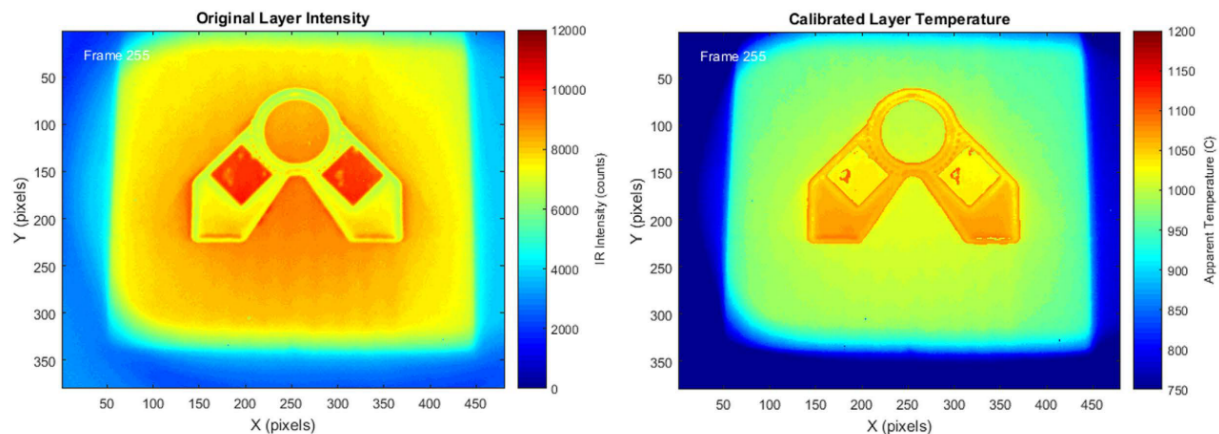


Figure 2. NIR temperature calibration. Left: original; right: calibrated. From [3].

These images can then be correlated to slices of the build file to locate porosity in the finished part. By collecting process log data and near infrared images for every layer, and correlating trends in porosity formation and mechanical performance, it was shown that the location of pores is heavily influenced by the cross-sectional area and correlates with the failure sites from uniaxial testing [4]. This analysis was performed using filters coded for Dream3.D, a data visualization platform developed at the Air Force Research Laboratory (AFRL). As shown in Figure 3, specific failure locations can be traced back to porosity data and ultimately to variation in powder feedstock [5]. Porosity location was also successfully

tracked during fabrication of topology-optimized parts, and shown to correlate with regions experiencing premature failure [6].

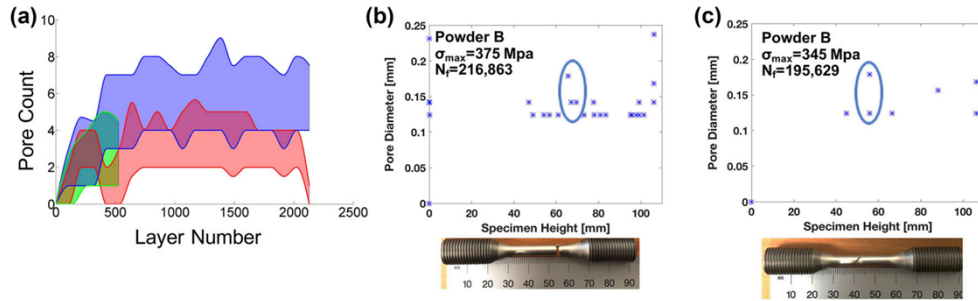


Figure 3. In-situ porosity detection. (a) Pore count per layer as a function of layer number for Powder B (shades of blue) having large number of pores per layer compared to Powders A (shades of red) and C (shades of green). (b, c) The correlation between pore diameter and failure site of the sample (Color figure online). (From [5]).

1.1.2 Data tools

To make use of the vast amounts of data generated during the EBM process, ORNL researchers have developed a number of data tools. Falcon, shown in Figure 4, is a new visual analytics system that allows users to interactively explore large, time-oriented data sets from multiple linked perspectives. Falcon provides overviews, detailed views, and unique segmented time series visualizations, all with adjustable scale options [7]. The goal is to allow discovery of patterns related to defects and system performance issues, optimization of build configurations to avoid defects, and to increase production efficiency.

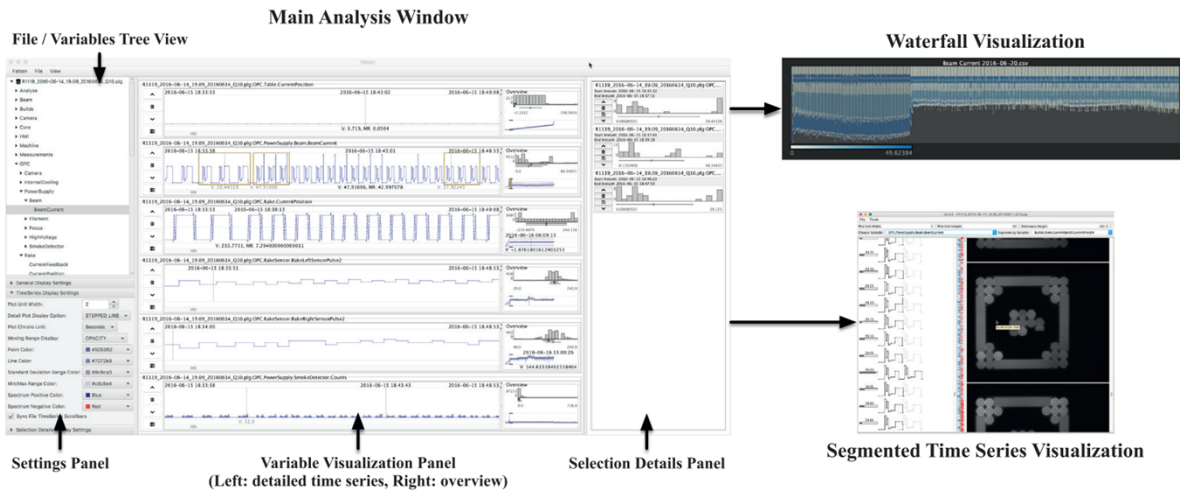


Figure 4. The main analysis window (left) in Falcon consists of a set of interactive data visualizations that allow users to explore temporal and statistical patterns in time series data for multiple variables. The center variable visualization panel features both overview and detail visualizations. When time range selections are set (see the three rectangles with yellow borders in the BeamCurrent variable pane), a statistical summary pane is added to the selection details panel at right to summarize the selected data. From the main window, the user can access two additional analysis windows, which provide more detailed views of segments derived from the entire time series of a particular variable.

The Exploratory Data ENvironment (EDEN), shown in Figure 5, allows visualization of trends in log file information via a parallel coordinates technique. Each line corresponds to a string of time-dependent variables, and data at a particular time step are linked across different variables. Changes in processing parameters between layers are therefore easily visualized and provide insight into the connectivity of various processing parameters.

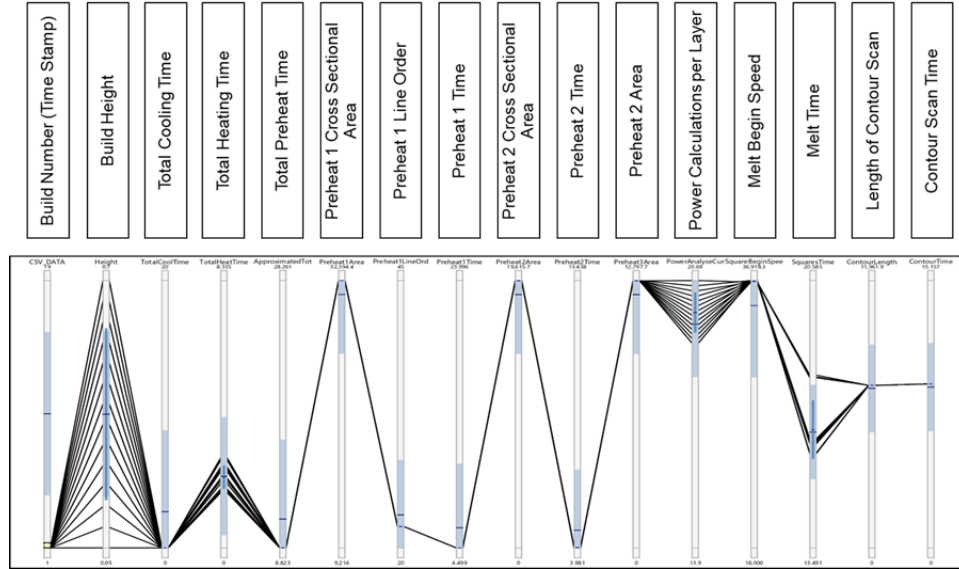


Figure 5: EDEN interface showing key variables.

1.2 MICROSTRUCTURE CONTROL

The highly localized layer-by-layer methodology of EBM processes allows for an unprecedented level of control over the microstructure of AM components. Texture is an important parameter for structural metallic components where crystallographic orientation can significantly influence properties, including elastic modulus, plastic deformation and thermal conductivity. For example, in gas turbine engines, nickel-base superalloys are used in single crystal and polycrystalline forms, depending on the desired mechanical properties and applications. Moreover, texture is closely related to grain boundary networks and attempts have been made at grain boundary engineering to control materials behavior. However, traditional metal part fabrication techniques have limited control to induce site specific grain size and crystallographic orientations due to their inability to control heat transfer conditions at very small length scales. With the emergence of powder bed metal AM techniques, new metallurgical engineering strategies can now be deployed to challenge traditional manufacturing paradigms.

Local microstructure is governed by spatial and temporal variations in thermal gradient (G) and solidification rate (R). While typical line scan melt strategies tend to result in parts with a strong (001) fiber texture in the build direction, a point source melt strategy can promote an equiaxed grain structure. The electron beam heat source can rapidly change between point and line heat source modes to promote steady state and/or transient thermal gradients and liquid/solid interface velocity. To demonstrate the possibility of site-specific microstructure control, an Inconel 718 part with equiaxed solidification in the regions bounding the letters D, O and E was fabricated [8]. The resulting part is shown in Figure 8. Bragg-edge neutron imaging was used to confirm that the desired microstructure extends through the thickness of the part, as neutrons are electronically charge-free and can achieve deep penetration, making them widely suitable for non-destructive evaluation.

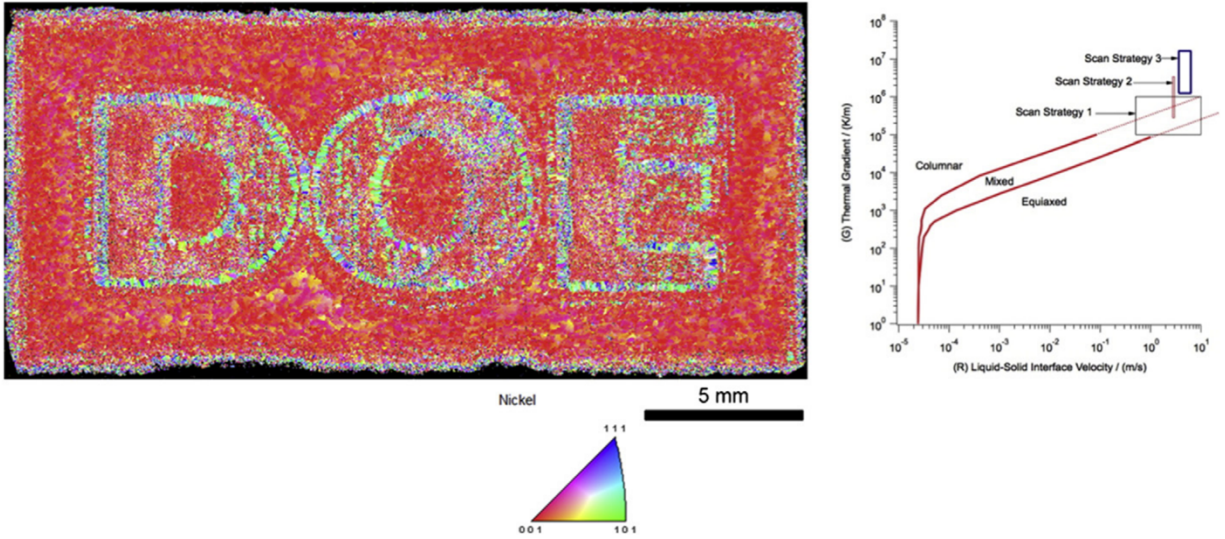


Figure 8. Crystallographic orientation map corresponding to inverse pole figure for fcc nickel obtained on cross-section of EBM build obtained through EBSD. The bulk shows $\langle 001 \rangle$ columnar solidification grain growth, the outline of the letters show equiaxed grain growth indicated by lack of any significant $\langle 001 \rangle$ component, and the interior areas of letters D, O and E exhibit a mixture of $\langle 001 \rangle$ growth with the solidification map for Inconel 718 describing the estimated ranges for G and R for each of scan strategies overlaid. From [9].

However, based on the black box algorithm of the EBM process, applying texture control over generic cross-sections within bulk structures in a controlled manner is extremely challenging. ORNL researchers therefore designed a point heat source melt strategy, shown in Figure 9, and compared it to the traditional raster (snake) scan strategy currently utilized for filling the melt area in the EBM process. Through this point heat source strategy, the ability to form either columnar or equiaxed grain structures upon solidification through changes in the process parameters associated with the point heat source fill was demonstrated for the Ni-base superalloy, Inconel 718. Mechanically, the material was demonstrated to exhibit either anisotropic properties for the columnar-grained material fabricated through using the standard raster scan of the EBM process or isotropic properties for the equiaxed material fabricated using the point heat source fill [10].

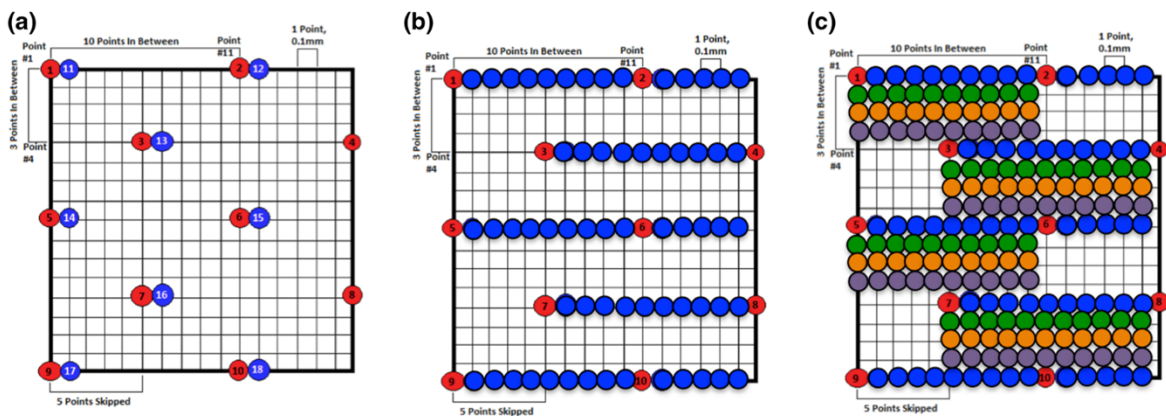


Figure 9. Exploded view of the point heat source fill detailing the fill of points. (a) the first and second points in each row set, (b) the fill of the first row set, (c) fill of subsequent rows. From [10].

Several modelling efforts have been undertaken to develop a deeper understanding of melt pool physics. An innovative scan strategy that splits the electron beam into a “melting” and “ghost” beam, analogous to beam splitting in welding, has been introduced into Electron Beam -Powder Bed Fusion (PBF) additive manufacturing to control solidification conditions. The influence of the ghost beam scan strategy on local thermal signatures was investigated in terms of melt pool shape, G and R. These numerical results show that it is indeed possible to induce targeted G and R in given geometry by employing standard-raster, spot-ordered, spot-consecutive and ghost beam strategies [11]. Modelling was also used to develop a novel melt scanning strategy optimized with a 3-D numerical model capable of predicting the fraction of equiaxed grain formation as a function of beam diameter, beam current, beam ON time, and preheat temperature. The model relies on the spatial and temporal calculation of thermal gradient (G) and liquid-solid interface velocity (R). The results of these calculations were then coupled with published criteria for columnar to equiaxed transition during solidification, as shown in Figure 10 [12].

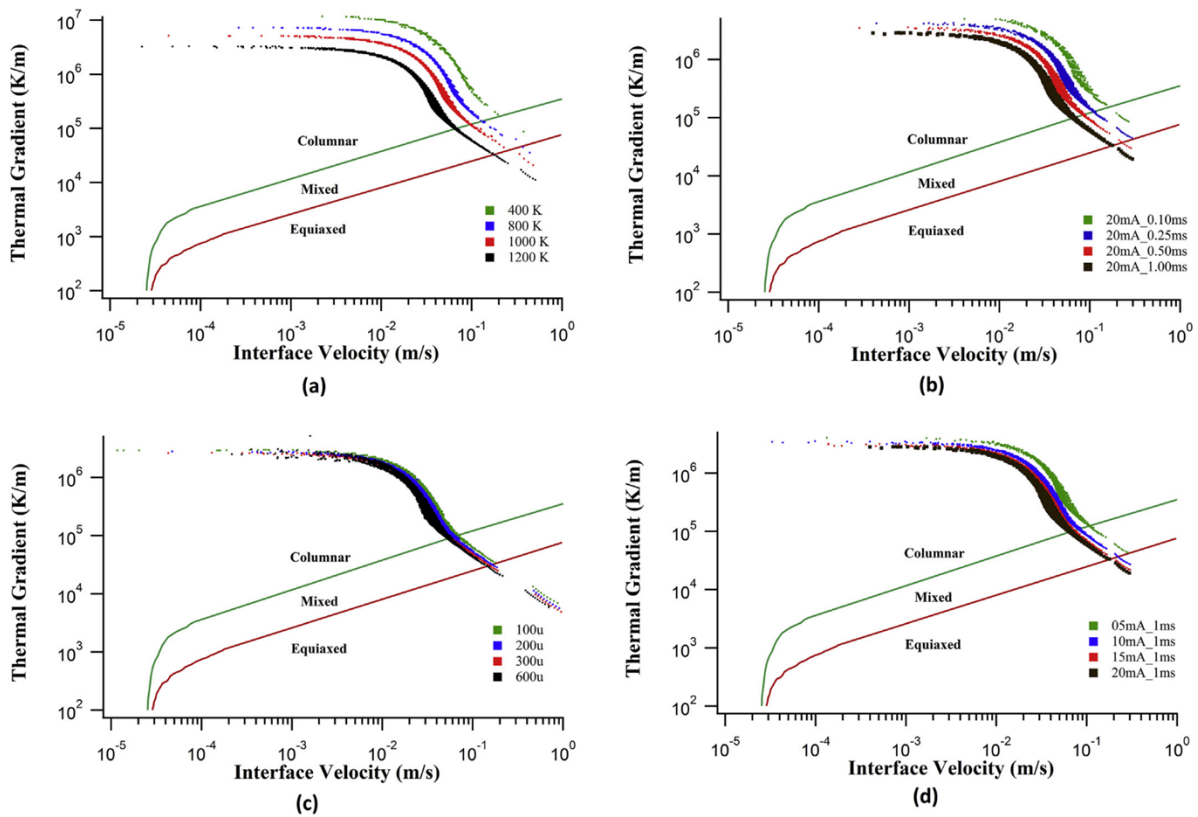


Figure 10. Change in temperature gradient (G) and liquid-solid interface velocity (R) of spot melt as a function of (a) preheat temperature, (b) spot ON time, (c) beam diameter, and (d) spot beam current. From [12].

Instead of switching between raster and spot melting pattern, microstructure can be controlled using a simple innovative approach of controlling only the spot-on time. The processing conditions were designed by using a simple heat transfer analytical model capable of predicting the spatial and temporal thermal signatures, as well as transient melt pool shapes. By varying only spot-on time, the majority of G and R values can be moved from below the CET (Columnar-Equiaxed Transition) line, suggesting equiaxed grain formation, to above the transition line, suggesting columnar grain formation. These results are shown in Figure 11.

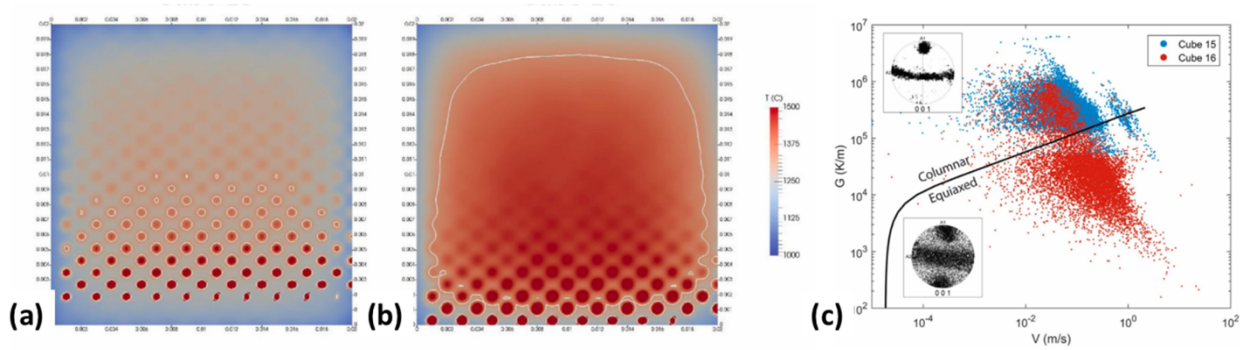


Figure 11. A snapshot of the simulated surface melt pools for the (a) cube 15 and (b) cube 16 processing conditions. (c) Values of predicted G and R overlaid on top of the CET curve for alloy 718. From [13].

ORNL researchers also explored the ability to control site-specific microstructure in a complex bracket geometry. A square region was selected for spot melting conditions and rest of the geometry was processed by standard raster conditions. The solidification grain structure of the brackets was analyzed using electron backscatter diffraction (EBSD) imaging along the build direction, as shown in Figure 12. The square regions melted with spot patterns consistently lead to equiaxed solidification texture and a grain size in the order of $\sim 100 \mu\text{m}$. In contrast, the ring region contained long, coarse ($\sim 300 \mu\text{m}$) columnar grains extending along the build direction. These results confirm the merit of simulation-aided process parameter and beam scanning strategy as a function of location to arrive at site-specific microstructure in a complex geometry made with nickel-base superalloy, and also emphasize the important role of in-situ monitoring in manufacturing successful components [3].

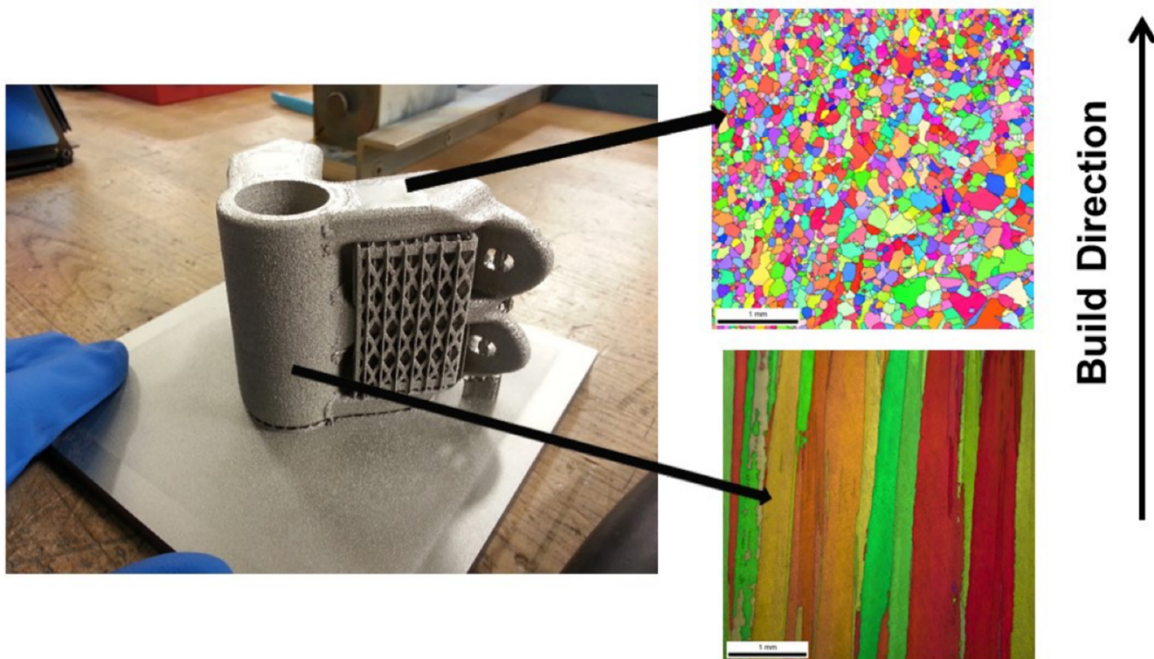


Figure 12. Completed EB-PBF alloy 718 bracket build with equiaxed grain formation in the spot melt region and columnar grain formation in the raster melt region. From [13].

1.3 HIGH-TEMPERATURE MATERIALS

Ti-6Al-4V is the most widely used and studied alloy for the EBM process. Some of this work has been performed by ORNL researchers, including studying fatigue crack growth [14], effects of heat treatment [14], fatigue behavior, and mapping pore structure using neutron diffraction [15]. Extension of the EBM process to nickel-base superalloys such as Inconel 718 has proven to be attractive for both aerospace and energy applications in terms of reducing the expensive casting, forging, and heat treatment operation. ORNL researchers therefore set out to establish a process routine for deposition of IN718 by EBM.

As the microstructure of AM components has a fundamental effect on its mechanical properties, considerable focus has been directed toward understanding the relationship between process parameters and the resulting microstructures in IN718 parts. During the electron beam melting (EBM) process, builds occur at temperatures in excess of 800°C for nickel-base superalloys such as Inconel 718. When coupled with the temporal differences between the start and end of a build, a top-to-bottom microstructure gradient forms, shown in Figure 13. This microstructural gradient is associated with a trend of increasing strength with height [16].

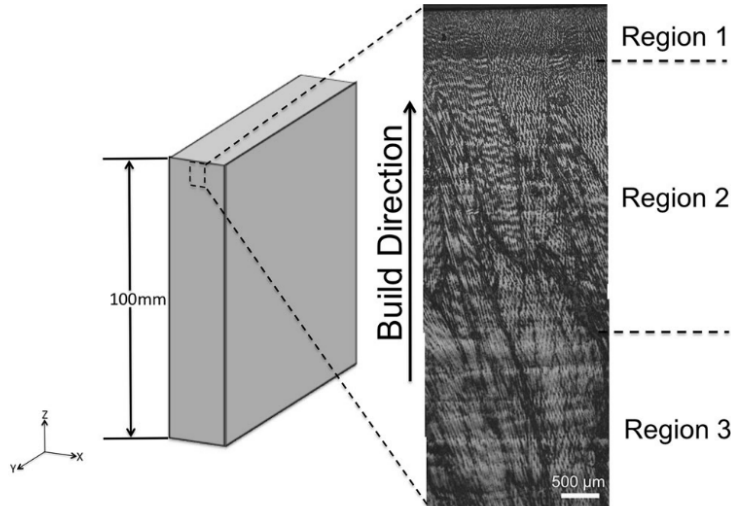


Figure 13. Optical micrograph of the microstructure gradient observed at the top of EBM Inconel 718 block with the three distinct regions discernible. From [16]

Post-processing methods play a particularly important role in EBM of IN718 parts, and are required to achieve the desired level of hardness. Because of the different heating processes involved, material made in an EBM process can be subjected to different thermal cycles, both axially and in bulk, leading to heterogenous microstructure [17]. After post-processing by hot isostatic pressing (HIP) and solution treatment and aging (STA), the yield strength, ultimate strength, and elongation at failure for the EBM Inconel 718 were observed to have beneficially increased compared to the as-fabricated material [18]. An investigation of the low-cycle fatigue (LCF) behavior showed that in all instances, the EBM HIP and heat-treated Inconel 718 performed similarly or exceeded the LCF life of wrought Inconel 718 plate and bar stock under fully reversed strain-controlled loading at 650°C [19]. The effects of post-processing also depend on the as-fabricated microstructure, as post-processing dissolves δ phase but not grain boundary carbides, and remaining carbides can therefore pin grain boundaries and prevent coarsening [20]. It is interesting to note that due to the multi-step nature of the EBM process, it may be possible to perform heat treatment inside the build chamber, negating the need for additional process steps [21].

While IN718 provides substantial gains in high-temperature strength compared to Ti-6Al-4V, its properties are rather modest when compared to other high-temperature alloys. Unfortunately, alloys with superior high-temperature strength are also considerably more difficult to process via AM due to their non-weldability. Alloys currently in use for critical rotating components for applications in gas turbine engines, such as IN738 and MarM247, are traditionally considered non-weldable and are highly susceptible to strain-age cracking, as shown in Figure 14.

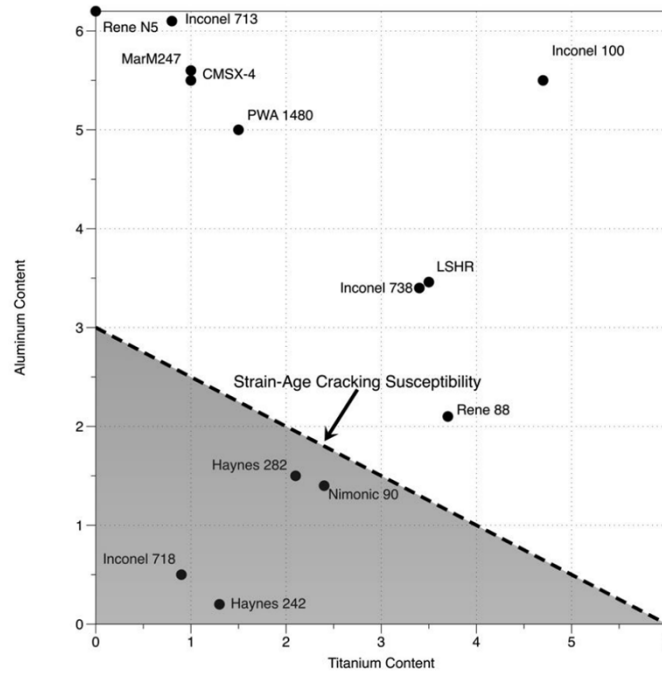


Figure 14. Aluminum and titanium content of common Ni-base superalloys in relation to their susceptibility to cracking.

Nevertheless, ORNL researchers were able to demonstrate successful EBM of several high-temperature alloys including Hastelloy X, Haynes 282, LSHR, IN738, and Mar-M247. Tensile properties of HIP'ed and heat-treated EBM Mar-M247 are shown in Figure 15 and confirm that EBM Mar-M247 is highly creep-resistant.

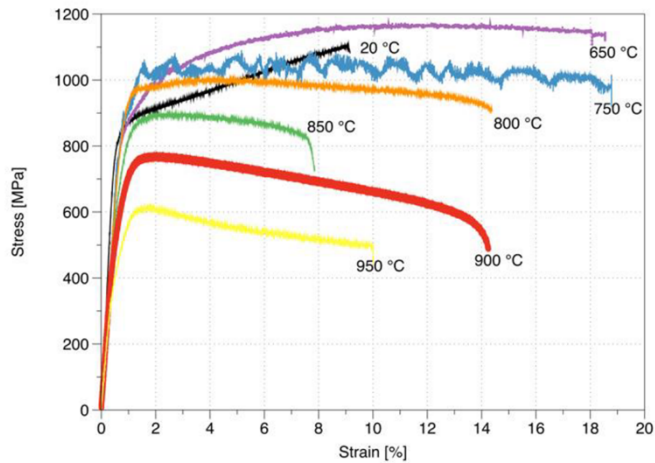


Figure 15. Tensile properties of post-processed EBM Mar-M247 at various temperature from room temperature through 950°C.

A modelling effort was undertaken to understand the role of cracking in these high γ' alloys. The cracking analysis was performed on cylindrical overhang structures where the cracks are observed only on one side of the part. Comprehensive microstructural characterization correlated the cracking tendency to low-melting point liquid-film formation along columnar grain boundaries with high misorientation angles due to partitioning of alloying elements. The simulations, shown in Figure 16, revealed asymmetric temperature distributions and associated asymmetric tensile thermal stresses over a cross section due to differences in section modulus and periodic changes in beam scanning directions. The results provide a potential pathway based on spatially varying beam scanning strategies to reduce the cracking tendency during additive manufacturing of complex geometries on the overhang structure in high-gamma prime nickel-based superalloys.

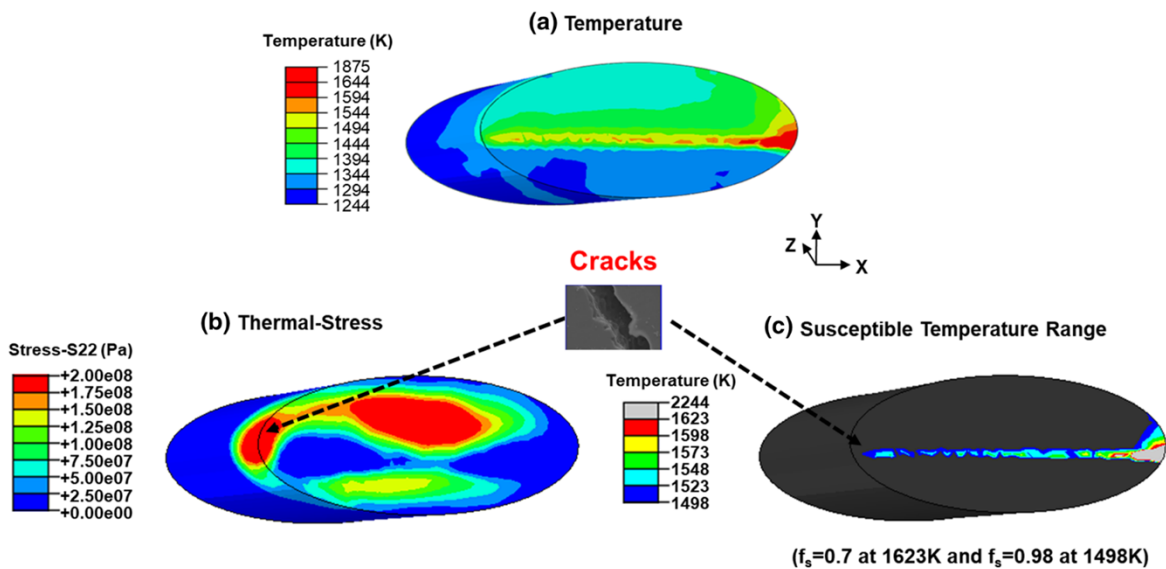


Figure 16. Evolution of (a) temperature distribution, (b) thermal stress (only tensile stresses are shown and therefore color images indicate as force imbalance), and (c) susceptible temperature range ($f_s = 0.7$ at 1623 K and $f_s = 0.98$ at 1498 K) during horizontal scanning. Hot cracking occurs at the intersection of the susceptible temperature range and high at the left edge (S22 is along y-direction). From [22].

1.4 SUMMARY

In collaboration with Arcam AB, ORNL researchers have improved the reliability of EBM processes, increased control over EBM component microstructures, and expanded EBM methodologies to new high-temperature materials such as Inconel 718 and MarM247. Development of in-situ monitoring techniques and data analytics tools have made qualification and certification of EBM components possible. Novel melt scan strategies have allowed ORNL researchers to manufacture components with site-specific microstructure control, enabling an unprecedented ability to tailor component properties to meet design needs. Finally, development of EBM processing parameters for high-temperature nickel-base superalloys has allowed ORNL researchers to manufacture critical rotating components such as turbine blades using EBM.

1.4.1 Subject Inventions

There are no subject inventions associated with this CRADA.

1.4.2 Publications

See the following sections for publications resulting from this work. Other publications generated during this CRADA, but not cited above: [23], [24], [33]–[42], [25], [43]–[48], [26]–[32]

2. PUBLICATIONS

- [1] R. R. Dehoff *et al.*, “In preparation for the International Journal of Fluid Power FREEFORM FLUIDICS In preparation for the International Journal of Fluid Power,” *Int. J. Fluid Power*, vol. 1, no. 2, pp. 17–22, 2013.
- [2] R. Dehoff *et al.*, “Case Study: Additive Manufacturing of Aerospace Brackets,” 2013.
- [3] J. Raplee *et al.*, “Thermographic Microstructure Monitoring in Electron Beam Additive Manufacturing,” *Sci. Rep.*, vol. 7, no. October 2016, pp. 1–16, 2017.
- [4] S. Yoder *et al.*, “Approach to Qualification using E-PBF In-situ Processes Monitoring in Ti-6Al-4V.” 2018.
- [5] P. Nandwana, M. M. Kirka, V. C. Paquit, S. Yoder, and R. R. Dehoff, “Correlations Between Powder Feedstock Quality, In Situ Porosity Detection, and Fatigue Behavior of Ti-6Al-4V Fabricated by Powder Bed Electron Beam Melting: A Step Towards Qualification,” *JOM*, vol. 70, no. 9, pp. 1686–1691, 2018.
- [6] S. Yoder *et al.*, “Characterization of topology optimized Ti-6Al-4V components using electron beam powder bed fusion,” *Addit. Manuf.*, vol. 19, pp. 184–196, 2018.
- [7] C. A. Steed, W. Halsey, R. Dehoff, S. L. Yoder, V. Paquit, and S. Powers, “Falcon: Visual analysis of large, irregularly sampled, and multivariate time series data in additive manufacturing,” *Comput. Graph.*, vol. 63, pp. 50–64, 2017.
- [8] R. R. Dehoff *et al.*, “Site specific control of crystallographic grain orientation through electron beam additive manufacturing,” *Mater. Sci. Technol.*, vol. 31, no. 8, pp. 931–938, 2015.
- [9] M. M. Kirka, P. Nandwana, Y. Lee, and R. R. Dehoff, “Solidification and solid-state transformation sciences in metals additive manufacturing,” *Scr. Mater.*, vol. 135, pp. 130–134, 2017.
- [10] M. M. Kirka *et al.*, “Erratum to: Strategy for Texture Management in Metals Additive Manufacturing (*JOM*, (2017), 69, 3, (523-531), 10.1007/s11837-017-2264-3),” *JOM*, vol. 69, no. 5, p. 948, 2017.
- [11] Y. S. Lee *et al.*, “Role of scan strategies on thermal gradient and solidification rate in electron beam powder bed fusion,” *Addit. Manuf.*, vol. 22, no. April, pp. 516–527, 2018.
- [12] N. Raghavan *et al.*, “Corrigendum to ‘Numerical modeling of heat-transfer and the influence of process parameters on tailoring the grain morphology of IN718 in electron beam additive manufacturing’ [*Acta Mater.* 112C (2016) 303–314], (S1359645416302294), (10.1016/j.actamat.2016,” *Acta Mater.*, vol. 140, p. 472, 2017.
- [13] S. S. Babu *et al.*, “Additive Manufacturing of Nickel Superalloys: Opportunities for Innovation and Challenges Related to Qualification,” *Metall. Mater. Trans. A Phys. Metall. Mater. Sci.*, vol. 49, no. 9, pp. 3764–3780, 2018.
- [14] H. Galarraga, R. J. Warren, D. A. Lados, R. R. Dehoff, and M. M. Kirka, “Fatigue crack growth mechanisms at the microstructure scale in as-fabricated and heat treated Ti-6Al-4V ELI manufactured by electron beam melting (EBM),” *Eng. Fract. Mech.*, vol. 176, pp. 263–280, 2017.
- [15] A. J. Brooks *et al.*, “Porosity detection in electron beam-melted Ti-6Al-4V using high-resolution neutron imaging and grating-based interferometry,” *Prog. Addit. Manuf.*, vol. 2, no. 3, pp. 125–132, 2017.
- [16] M. M. Kirka, K. A. Unocic, N. Raghavan, F. Medina, R. R. Dehoff, and S. S. Babu, “Microstructure Development in Electron Beam-Melted Inconel 718 and Associated Tensile Properties,” *JOM*, vol. 68, no. 3, pp. 1012–1020, 2016.
- [17] W. J. Sames, K. A. Unocic, R. R. Dehoff, T. Lolla, and S. S. Babu, “Thermal effects on microstructural heterogeneity of Inconel 718 materials fabricated by electron beam melting,” *J. Mater. Res.*, vol. 29, no. 17, pp. 1920–1930, 2014.
- [18] M. M. Kirka, F. Medina, R. Dehoff, and A. Okello, “Mechanical behavior of post-processed

- Inconel 718 manufactured through the electron beam melting process,” *Mater. Sci. Eng. A*, vol. 680, no. October 2016, pp. 338–346, 2017.
- [19] M. M. Kirka, D. A. Greeley, C. Hawkins, and R. R. Dehoff, “Effect of anisotropy and texture on the low cycle fatigue behavior of Inconel 718 processed via electron beam melting,” *Int. J. Fatigue*, vol. 105, pp. 235–243, 2017.
- [20] P. Nandwana, M. Kirka, A. Okello, and R. Dehoff, “Electron beam melting of Inconel 718: effects of processing and post-processing,” *Mater. Sci. Technol.*, vol. 34, no. 5, pp. 612–619, 2018.
- [21] W. J. Sames *et al.*, “Feasibility of in situ controlled heat treatment (ISHT) of Inconel 718 during electron beam melting additive manufacturing,” *Addit. Manuf.*, vol. 13, pp. 156–165, 2017.
- [22] Y. S. Lee *et al.*, “Asymmetric Cracking in Mar-M247 Alloy Builds During Electron Beam Powder Bed Fusion Additive Manufacturing,” *Metall. Mater. Trans. A Phys. Metall. Mater. Sci.*, pp. 1–15, 2018.
- [23] Z. Bi *et al.*, “Self-organized amorphous TiO₂ nanotube arrays on porous Ti foam for rechargeable lithium and sodium ion batteries,” *J. Power Sources*, vol. 222, pp. 461–466, 2013.
- [24] T. Watkins *et al.*, “Neutron Characterization for Additive Manufacturing,” *Adv. Mater. Process.*, vol. 171, no. 3, pp. 23–27, 2013.
- [25] S. S. Babu, L. Love, R. Dehoff, W. Peter, T. R. Watkins, and S. Pannala, “Additive manufacturing of materials: Opportunities and challenges,” *MRS Bull.*, vol. 40, no. 12, pp. 1154–1161, 2015.
- [26] R. R. Dehoff, M. M. Kirka, F. A. List, K. A. Unocic, and W. J. Sames, “Crystallographic texture engineering through novel melt strategies via electron beam melting: Inconel 718,” *Mater. Sci. Technol.*, vol. 31, no. 8, pp. 939–944, 2015.
- [27] P. Nandwana *et al.*, “Recyclability Study on Inconel 718 and Ti-6Al-4V Powders for Use in Electron Beam Melting,” *Metall. Mater. Trans. B*, vol. 47, no. 1, 2015.
- [28] P. Prabhakar, W. J. Sames, R. Dehoff, and S. S. Babu, “Computational modeling of residual stress formation during the electron beam melting process for Inconel 718,” *Addit. Manuf.*, vol. 7, pp. 83–91, 2015.
- [29] L. M. Sochalski-Kolbus *et al.*, “Comparison of Residual Stresses in Inconel 718 Simple Parts Made by Electron Beam Melting and Direct Laser Metal Sintering,” *Metall. Mater. Trans. A Phys. Metall. Mater. Sci.*, vol. 46, no. 3, pp. 1419–1432, 2015.
- [30] H. Z. Bilheux *et al.*, “Advances in Neutron Radiography : Application to Additive Manufacturing Inconel 718,” *Adv. Mater. Process.*, 2016.
- [31] H. Bilheux *et al.*, “Neutron Characterization of Additively Manufactured Inconel 718,” *Adv. Mater. Process.*, vol. 175, p. 16, 2016.
- [32] E. Cakmak *et al.*, “Microstructural and micromechanical characterization of IN718 theta shaped specimens built with electron beam melting,” *Acta Mater.*, vol. 108, pp. 161–175, 2016.
- [33] E. Cakmak *et al.*, “Mechanical Characterization of an Additively Manufactured Inconel 718 Theta-Shaped Specimen,” *Metall. Mater. Trans. A Phys. Metall. Mater. Sci.*, vol. 47, no. 2, pp. 971–980, 2016.
- [34] H. Galarraga, D. A. Lados, R. R. Dehoff, M. M. Kirka, and P. Nandwana, “Effects of the microstructure and porosity on properties of Ti-6Al-4V ELI alloy fabricated by electron beam melting (EBM),” *Addit. Manuf.*, vol. 10, pp. 47–57, 2016.
- [35] J. Mo, R. R. Dehoff, W. H. Peter, T. J. Toops, J. B. Green, and F. Y. Zhang, “Additive manufacturing of liquid/gas diffusion layers for low-cost and high-efficiency hydrogen production,” *Int. J. Hydrogen Energy*, vol. 41, no. 4, pp. 3128–3135, 2016.
- [36] W. J. Sames, F. A. List, S. Pannala, R. R. Dehoff, and S. S. Babu, “The metallurgy and processing science of metal additive manufacturing,” *Int. Mater. Rev.*, vol. 61, no. 5, pp. 315–360, 2016.
- [37] Z. C. Cordero, R. B. Dinwiddie, D. Immel, and R. R. Dehoff, “Nucleation and growth of chimney pores during electron-beam additive manufacturing,” *J. Mater. Sci.*, vol. 52, no. 6, pp. 3429–3435, 2017.
- [38] Z. C. Cordero, H. M. Meyer, P. Nandwana, and R. R. Dehoff, “Powder bed charging during electron-beam additive manufacturing,” *Acta Mater.*, vol. 124, pp. 437–445, 2017.

- [39] H. Galarraga, R. J. Warren, D. A. Lados, R. R. Dehoff, M. M. Kirka, and P. Nandwana, “Effects of heat treatments on microstructure and properties of Ti-6Al-4V ELI alloy fabricated by electron beam melting (EBM),” *Mater. Sci. Eng. A*, vol. 685, pp. 417–428, 2017.
- [40] G. Song *et al.*, “Thermally-Induced Dynamic Evolution of Additively Manufactured Metal Microstructures,” 2017.
- [41] I. E. Anderson, E. M. H. White, and R. Dehoff, “Feedstock powder processing research needs for additive manufacturing development,” *Curr. Opin. Solid State Mater. Sci.*, vol. 22, no. 1, pp. 8–15, 2018.
- [42] S. Chandrasekar *et al.*, “Data-Driven Investigation of Recyclability of Metal Powders for Additive Manufacturing,” 2018.
- [43] A. T. Polonsky *et al.*, “Defects and 3D structural inhomogeneity in electron beam additively manufactured Inconel 718,” *Mater. Charact.*, no. 17, pp. 1–26, 2018.
- [44] Q. Xie *et al.*, “Applying neutron transmission physics and 3D statistical full-field model to understand 2D Bragg-edge imaging,” *J. Appl. Phys.*, vol. 123, no. 7, 2018.
- [45] A. Plotkowski, B. Stump, J. Heigel, R. E. Ricker, L. Levine, and R. R. Dehoff, “A Transient Analytical Heat Conduction Model for Additive Manufacturing with Consideration for Latent Heat.” 2018.
- [46] B. Shassere, D. Greely, A. Okello, M. Kirka, and R. Dehoff, “Correlation of Microstructure to Creep Response of Hot Isostatically Pressed and Aged Electron Beam Melted Inconel 718.” 2018.
- [47] G. Song *et al.*, “Using Bragg-Edge Neutron Imaging to Characterize Crystallographic Structure of Additively Manufactured Inconel 718 Components.” 2018.
- [48] Q. Xie *et al.*, “Investigating the lattice strain evolution of polycrystalline Inconel 718 with strong cube texture using in-situ neutron diffraction and crystal plasticity based modeling.” 2018.